ORIGINAL PAPER

Electrochemical performance of Sn-doped cobalt-free Li$_{1.15}$Ni$_{0.27}$Mn$_{0.58-x}$Sn$_x$O$_2$ cathode material for Li-ion batteries

Hui Li[1] · Zhenye Zhu[1,2] · Jiaheng Zhang[1,2] · Huang Qin[1] · Yuanbo Tan[1,2] · Xueting Zhang[1,2] · Zhixiong Yang[1,2] · Guangxing Pan[1,2] · Wanbao Wu[1,2] · Mingjie Yi[1,2] · Shunyou Hu[1,2] · Ke Qin[1,2] · Miaomiao Chao[1,2]

Abstract

In this study, a series of cobalt-free Sn-doped cathode materials of Li$_{1.15}$Ni$_{0.27}$Mn$_{0.58-x}$Sn$_x$O$_2$ are prepared by the solvothermal method for the first time. The structural characterization of the material reveals that all the samples consist of hexagonal layered structural LiMO$_2$ (M = Mn/Ni), monoclinic-layered structural Li$_2$MnO$_3$, and cubic spinel structural LiMn$_2$O$_4$. Moreover, the interplanar spacing of the layered structure increases in the material, and the electrochemical impedance of the material declines by Sn doping. As a result, all Sn-doped samples exhibit better electrochemical performance than pristine Li$_{1.15}$Ni$_{0.27}$Mn$_{0.58}$O$_2$ materials. Among them, Li$_{1.15}$Ni$_{0.27}$Mn$_{0.56}$Sn$_{0.02}$O$_2$ delivers comprehensively improved electrochemical performance. The initial coulombic efficiency of the Li$_{1.15}$Ni$_{0.27}$Mn$_{0.56}$Sn$_{0.02}$O$_2$ sample is 84.4%, which is nearly 10% higher than the pristine material, and Li$_{1.15}$Ni$_{0.27}$Mn$_{0.56}$Sn$_{0.02}$O$_2$ exhibits an initial discharge specific capacity of 260.8 mAh/g at a current density of 0.1 C, and the capacity retention after first 100 cycles at 1 C reached 94.67%. Rate capability of Li$_{1.15}$Ni$_{0.27}$Mn$_{0.58-x}$Sn$_x$O$_2$ is significantly improved by Sn doping. The specific discharge capacity of the Li$_{1.15}$Ni$_{0.27}$Mn$_{0.56}$Sn$_{0.02}$O$_2$ sample at 5 C is two times higher than that of Li$_{1.15}$Ni$_{0.27}$Mn$_{0.58}$O$_2$. Moreover, the Li$_{1.15}$Ni$_{0.27}$Mn$_{0.56}$Sn$_{0.02}$O$_2$ material can still maintain a discharge capacity of 220 mAh/g when the current density returns to 0.1 C after a large current density cycling process. These results show that the proper amount of Sn doping can effectively improve the electrochemical performance of Li$_{1.15}$Ni$_{0.27}$Mn$_{0.58}$O$_2$, due to the fact that Sn ions have larger ionic radii than the transition metal (Mn/Ni) ions and Sn can partially replace the transition metal element ions in the layered structure, thereby expanding the lithium ion diffusion channel and inhibiting instability of the material structure during the cycle. However, an excessive amount of Sn (x > 0.03) generates a Li$_2$SnO$_3$ impurity in the material, resulting in deterioration of material properties.

Keywords Li-ion batteries · Co-free · Cathode material · Sn-doping · Rate capability

Hui Li, Zhenye Zhu, Jiaheng Zhang, and Huang Qin contributed equally to this paper.

Electronic supplementary material The online version of this article (https://doi.org/10.1007/s11581-020-03543-3) contains supplementary material, which is available to authorized users.

✉ Zhenye Zhu
zhuzy@hit.edu.cn

✉ Jiaheng Zhang
zhangjiaheng@hit.edu.cn

1   School of Materials Science and Engineering, Harbin Institute of Technology, Shen Zhen, Harbin 518055, China

2   Research Centre of Printed Flexible Electronics, School of Materials Science and Engineering, Harbin Institute of Technology, Shen Zhen, Harbin 518055, China

Introduction

The lithium-rich manganese-based cathode material xLi$_2$MnO$_3$·(1-x)LiMO$_2$ (0< x <1, M = Mn, Ni, Co) has a specific capacity of 250 mAh/g, an operating voltage exceeding 4.5 V, and a high energy density [1]. Currently, Co-free lithium-rich manganese-based cathode materials are generating widespread interest, due to their low cost and environmental friendliness [2, 3]. The lithium-rich manganese-based material can be considered as a matrix of layered Li$_2$MnO$_3$ and layered LiMO$_2$ (M = Mn, Ni, Co) forming a solid solution. Li$_2$MnO$_3$ and LiMO$_2$ are layered rock salt structures, similar to the structure of α-NaFeO$_2$, and Li$_2$MnO$_3$ can also be described in the form of Li[Li$_{1/3}$Mn$_{2/3}$]O$_2$. Therefore, the lithium-rich manganese-based cathode material xLi$_2$MnO$_3$.(1-x)LiMO$_2$ can be regarded as derived from layered Li$_2$MnO$_3$, in which

a part of the transition metal M replaces Li^+ in $Li[Li_{1/3}Mn_{2/3}]O_2$. However, the Li_2MnO_3 component in the material undergoes an irreversible structural change during charge and discharge, which results in poor performance during charge–discharge cycles. The main property deficiencies in lithium-rich manganese-based materials are as follows: the large capacity loss during the first charge and discharge process, poor rate capability, and unsatisfactory cycle performance. Elemental doping is considered as an effective way to improve the electrochemical properties of lithium-rich manganese-based materials [4].

Usually, an element with ionic radius close to the ions of the substituted elements is selected to dope in lithium-rich cathode materials. Element doping can improve the conductivity of the material, increase the lattice parameters, form stronger M–O bonds, which promotes Li^+ migration, and thus can significantly improve the structural stability and rate performance of the material. Doping methods include anionic doping, cationic doping, and anion–cation co-doping.

Anion doping generally selects F^- and S^{2-} to partially replace oxygen. Partial substitution of oxygen in the $Li[Li_{1/6}Ni_{1/4}Mn_{7/12}]O_{2-x}F_x$ material by fluorine can facilitate the growth of primary particles [5]. With increasing fluorine content, the cycle performance significantly improves. This is because fluorine substitution reduces irreversible oxygen loss in the lattice during the first cycle and promotes the formation of a layered-spinel symbiotic structure in the material. $Li_{1.2}Mn_{0.6}Ni_{0.2}O_{1.97}S_{0.03}$ obtained by substituting oxygen with a small amount of sulfur shows extremely high coulombic efficiency in the first cycle [6], due to reversible intercalation and deintercalation of Li^+ in S-doped materials.

Cation doping elements are generally used to replace the position of Mn in the material, and Li is substituted by Na^+ and K^+. Na^+ and Al^{3+} double doping can inhibit the side reaction between the $Na_xLi_{1.2-x}Mn_{0.6-x}Al_xNi_{0.2}O_2$ lithium-rich electrode and the electrolyte during the cycle [7], which greatly improves the high-temperature cycle stability of the material. Different from the nickel doping of the general lithium-rich manganese-based cathode material, only doping a small amount of nickel into $Li[Li_{1/3-2x/3}Mn_{2/3-x/3}Ni_x]O_2$ material can promote the progressive activation of Li_2MnO_3 [8], thereby obtaining a larger specific capacity and better cycle performance. In contrast, excess Ni overactivates Li_2MnO_3 and causes a large capacity loss in the first cycle. Cr doping in $Li_{1.1}Ni_{0.25}Mn_{0.75}O_{2.3}$ not only can effectively reduce the voltage attenuation [9] but also reduces the R_{ct} (charge transfer resistance) of the material, thus improving the cycle performance. In addition, Cr doping can reduce the content of Mn^{3+} in $Li_{1.2}Ni_{0.2}Mn_{0.6}O_2$ during the cycling process [10], thereby inhibiting the formation of the spinel-like structure and facilitating the increase in intermediate voltage. Moreover, Cr doping increases the lithium ion diffusion coefficient and electron conductivity of the $Li_{1.2}Ni_{0.2}Mn_{0.6}O_2$ cathode material,

thereby improving the rate performance. Adding a small amount of B^{3+} ions to the tetrahedral site in Li-rich material can prevent the transition metal ions in the material from migrating to the tetrahedral position [11], and can stabilize the material structure. Mg substitution in lithium-rich materials can increase the interlayer spacing and the lithium ion diffusion coefficient of the material [12], which significantly improves the insertion and deintercalation of lithium ions, rate capability, and cycle performance. In addition, Nb [13] or Y [14] substitution in lithium-rich materials has a similar effect to Mg. Zn substitution in lithium-rich materials reduces charge transfer resistance and increases exchange current density [15], improving the cycling performance, because of excellent structural stability and conductivity of the active electrode. Zr doping in lithium-rich materials can increase the lattice parameters and the structural stability of materials and suppress electrode polarization [16]. Moreover, Zr-doped lithium-rich materials have better cycle stability at large current densities, so the enhanced electrochemical performance is ascribed to the improved structural stability and lithium ion diffusion of bulk electrode materials. In summary, elements with a larger ionic radius can be used to replace transition metal elements in lithium-rich manganese-based materials, and they can generally increase the interplanar spacing without drastically changing the material structure.

In this work, we partially substituted Mn in the lithium-rich manganese-based cathode material $Li_{1.15}Ni_{0.27}Mn_{0.58}O_2$ with Sn. Sn has a larger ionic radius than Mn and Ni, which may improve the material structure and thus the material electrochemical performance. Although many researchers have tried to modify the positive electrode material with Sn, its mechanism of action is still unclear and worthy of further investigation.

Experimental methods

Synthesis of $Li_{1.15}Ni_{0.27}Mn_{0.58-x}Sn_xO_2$ ($x = 0$, 0.01, 0.02, 0.03, 0.04, 0.05) materials

$Li_{1.15}Ni_{0.27}Mn_{0.58-x}Sn_xO_2$ ($x = 0$, 0.01, 0.02, 0.03, 0.04, 0.05) cathode materials were synthesized by the solvothermal method. Three solutions were prepared. First, manganese acetate and nickel acetate were dissolved in ethanol together with tin acetate according to the molar ratio in the target material $Li_{1.15}Ni_{0.27}Mn_{0.58-x}Sn_xO_2$ and mechanically stirred until completely dissolved. Then, an appropriate amount of oxalic acid was dissolved in ethanol by ultrasonication. Finally, 5 wt% excess of lithium acetate was dissolved in ethanol by ultrasonication according to the molar ratio in the $Li_{1.15}Ni_{0.27}Mn_{0.58-x}Sn_xO_2$ material, where excess lithium was used to compensate for the loss of lithium during calcination.

The prepared oxalic acid and lithium acetate solution was added dropwise to the metal cation ethanol solution at room temperature, followed by continuous stirring for 8 h. Then, the mixture was subjected to a solvothermal reaction in a reaction vessel at 200 °C for 20 h.

After naturally cooling to room temperature, the reacted solution was stirred and evaporated in a water bath at 80 °C to obtain a precursor. After the precursor was treated with 450 °C pre-calcination and 650 °C high-temperature calcination in a furnace, the target $Li_{1.15}Ni_{0.27}Mn_{0.58-x}Sn_xO_2$ material was obtained.

Structure and morphology analysis

X-ray powder diffraction (XRD, Rigaku D/max-2500PC) with Cu K_α radiation (40 kV, 200 mA) between 10 and 80° with a scan rate of 5° min^{-1} was employed to analyze the phase composition and crystal structure of the as-prepared material. The morphology and particle size of $Li_{1.15}Ni_{0.27}Mn_{0.58-x}Sn_xO_2$ ($x = 0.01, 0.02, 0.03$) materials were analyzed by scanning electron microscopy (SEM, Hitachi S4700). X-ray photoelectron spectroscopy (XPS, PHI 5000 VersaProbe II, Al-Ka) was used to detect the valence states of transition metal elements (Mn and Ni) and Sn in $Li_{1.15}Ni_{0.27}Mn_{0.58-x}Sn_xO_2$ samples. In addition, the lattice fringes and microstructure of $Li_{1.15}Ni_{0.27}Mn_{0.58-x}Sn_xO_2$ materials were observed by transmission electron microscopy (TEM, Tecnai G2 Spirit, 120 kV).

Electrochemical measurements

The prepared cathode material $Li_{1.15}Ni_{0.27}Mn_{0.58-x}Sn_xO_2$ was sufficiently dissolved in N-Methyl pyrrolidone (NMP) solvent with polyvinylidene fluoride (PVDF) binder and carbon black at a weight ratio of 8:1:1 to prepare a slurry, which was coated on aluminum foil, dried, and then cut into an electrode. Subsequently, the electrode was assembled into a CR2032 coin cell with a lithium anode and a Celgard 2320 separator in a glove box for electrochemical performance testing. A 1 M LiPF6 solution (solvent is a mixture of ethylene carbonate (EC) and dimethyl carbonate (DMC) with volume ratio 1:1) was used as the electrolyte.

Results and discussion

Morphology and structure analysis

SEM images in Fig. 1 show that all the secondary particles of Sn-doped $Li_{1.15}Ni_{0.27}Mn_{0.58-x}Sn_xO_2$ samples exhibit loose aggregate morphology with many pores in their structure, and their sizes are similar with radii of approximately 1–2 μm. The primary particle of all samples is approximately 40 nm and is uniform in diameter. This fine-particle structure with loose pores facilitates the reaction of the electrode material with the electrolyte and the bulk transport of lithium ions.

The XRD patterns of different contents of Sn-doped samples of $Li_{1.15}Ni_{0.27}Mn_{0.58-x}Sn_xO_2$ ($x = 0, 0.01, 0.02, 0.03, 0.04, 0.05$) are shown in Fig. 2. Compared with the $Li_{1.15}Ni_{0.27}Mn_{0.58}O_2$ sample, there is no obvious change in the diffraction peaks of Sn-doped samples, and no new diffraction peaks appeared in the diffraction pattern of the samples with $x = 0.01$ and $x = 0.02$; however, two new weak diffraction peaks emerged in the material when $x \geq 0.03$. These new diffraction peaks belong to Li_2SnO_3, because excess Sn forms a Li_2SnO_3 heterophase in $Li_{1.15}Ni_{0.27}Mn_{0.58-x}Sn_xO_2$ cathode material. The diffraction peaks (400) and (511) of the cubic spinel phase appear in the spectrum of all $Li_{1.15}Ni_{0.27}Mn_{0.58-x}Sn_xO_2$ materials, indicating the presence of the spinel phase $LiMn_2O_4$ in the material. Additionally, the two pairs of (006)/(102) and (108)/(110) diffraction peaks are clearly split, which proves that $Li_{1.15}Ni_{0.27}Mn_{0.58-x}Sn_xO_2$ materials still maintain the $LiMO_2$ ($M = Mn, Ni$) layered structure [17]. In addition, the weak diffraction peaks of monoclinic Li_2MnO_3 phase appeared in all $Li_{1.15}Ni_{0.27}Mn_{0.58-x}Sn_xO_2$ samples between 20 and 25° [18]. Furthermore, with increasing Sn content, the positions of (003) and (104) diffraction peaks shift to a small angle, which signals an increase in the lattice constant of Sn-doped samples [19].

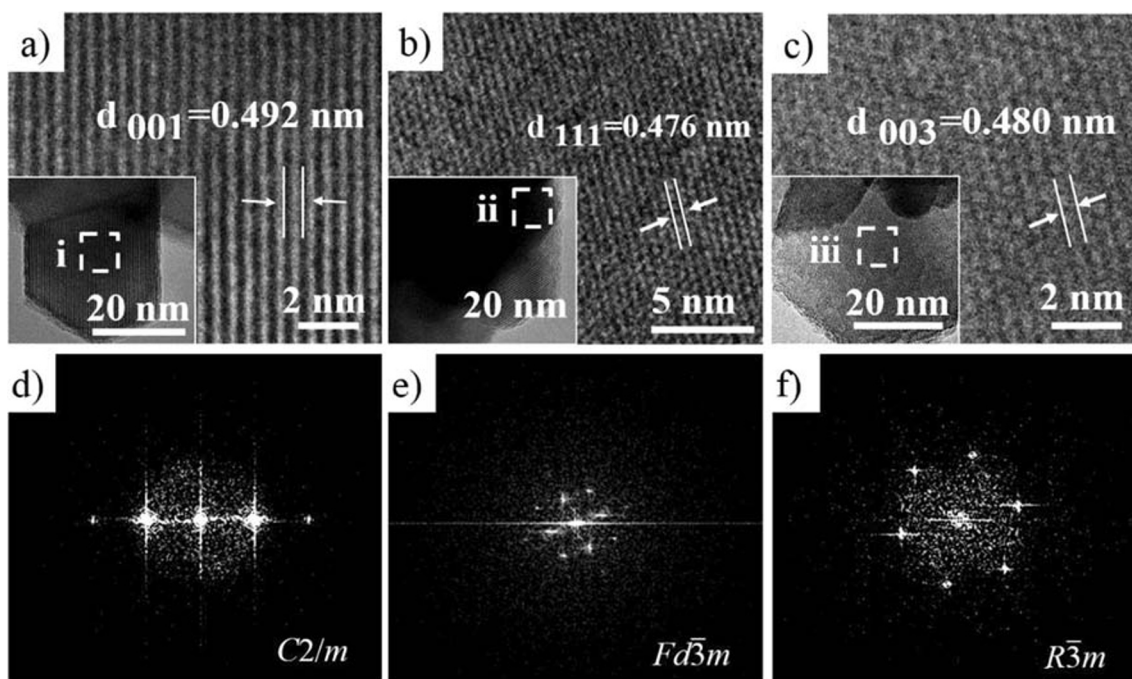Fig. 1 SEM images of $Li_{1.15}Ni_{0.27}Mn_{0.58-x}Sn_xO_2$ materials
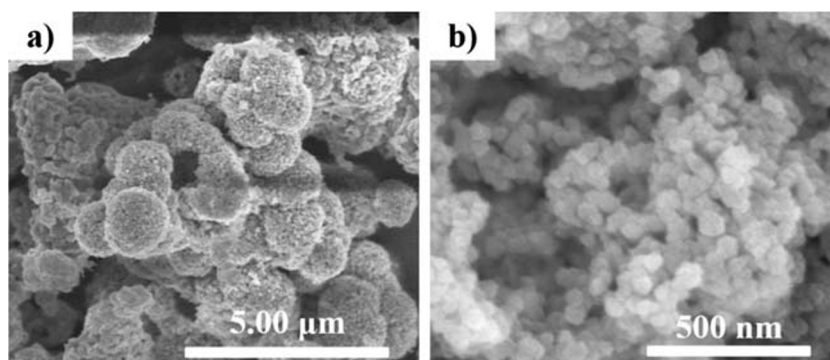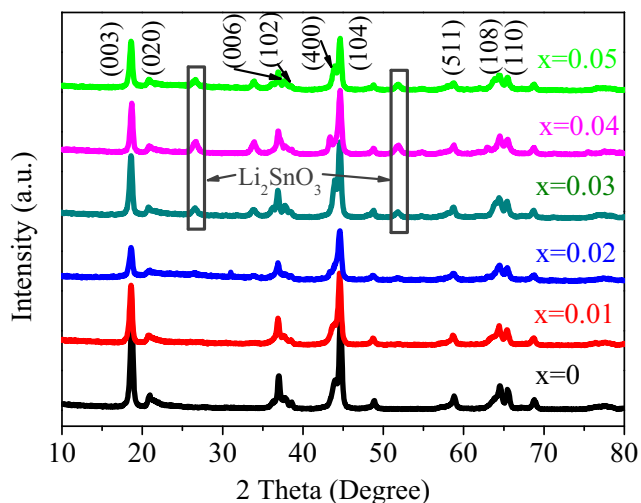
Fig. 2 XRD patterns of $Li_{1.15}Ni_{0.27}Mn_{0.58-x}Sn_xO_2$ materials

TEM characterization results of $Li_{1.15}Ni_{0.27}Mn_{0.56}Sn_{0.02}O_2$ ($x = 0.02$) are shown in Fig. 3. Figure 3a exhibits the HRTEM image of the i region with a crystal plane spacing of 0.492 nm. The fast Fourier transform (FFT) pattern of $Li_{1.15}Ni_{0.27}Mn_{0.56}Sn_{0.02}O_2$ in Fig. 3d characterizes a C2/m monoclinic-layered Li_2MnO_3 structure [20]. Figure 3 a and d demonstrates that the i region describes the (001) plane in the monoclinic structure. The interplanar spacing of the (001) plane in Fig. 3a increases compared with the pristine $Li_{1.15}Ni_{0.27}Mn_{0.58}O_2$ material (Fig. S1, 0.470 nm). The interplanar spacing of the ii region in Fig. 3b is 0.476 nm, and the FFT pattern of the ii region (Fig. 3e coincides with the

features of the $Fd\bar{3}$ m space group [21], showing that the ii region belongs to the (111) crystal plane of the spinel $LiMn_2O_4$ structure with $Fd\bar{3}$ m space group. The interplanar spacing of the iii region in Fig. 3c is 0.480 nm, which is slightly increased compared with the pristine $Li_{1.15}Ni_{0.27}Mn_{0.58}O_2$ material, and its FFT pattern conforms to the characteristics of the $R\bar{3}$ m hexagonal layered $LiMO_2$ structure [22], demonstrating that the iii region belongs to the (003) crystal plane in the layered structure. TEM characterization of $Li_{1.15}Ni_{0.27}Mn_{0.56}Sn_{0.02}O_2$ material indicates that the (001) plane interplanar spacing of the monoclinic-layered structure and the (003) plane of the hexagonal layered structure in the material increases, which is consistent with the XRD characterization results, proving that Sn enters the transition metal layer, while Sn ions with larger radii than the transition metal element ions Ni^{2+} and Mn^{4+} increase the interplanar spacing.

XPS analysis is performed on $Li_{1.15}Ni_{0.27}Mn_{0.58-x}Sn_xO_2$ cathode materials with different Sn contents to investigate the state of Sn in the material. The XPS spectra of $Li_{1.15}Ni_{0.27}Mn_{0.58-x}Sn_xO_2$ samples with $x = 0$ and $x = 0.05$ are shown in Fig. 4. Figure 4a shows the full XPS spectrum for $x = 0$ and $x = 0.05$ samples. Figure 4 b, c, and d illustrate XPS spectra of Mn_{2p}, Ni_{2p}, and Sn_{3d}. Compared with the pristine $Li_{1.15}Ni_{0.27}Mn_{0.58}O_2$ sample, Sn-doped samples show two new peaks at the binding energies of 494.5 eV and 486.5 eV (as shown in Fig. 4d), corresponding to Sn_{3d}, demonstrating that Sn exists in the form of Sn^{4+} [23]. In addition, the positions of other peaks in the spectra of $x = 0$ and $x = 0.05$ are similar; a pair of split $2p_{3/2}$ and $2p_{1/2}$ peaks appear in the spectrum of Mn and Ni [24]. The $2p_{3/2}$ peak at 642.1 eV

Fig. 3 TEM images of $Li_{1.15}Ni_{0.27}Mn_{0.56}Sn_{0.02}O_2$ materials (a)(b)(c) and corresponding FFT patterns (d)(e)(f)
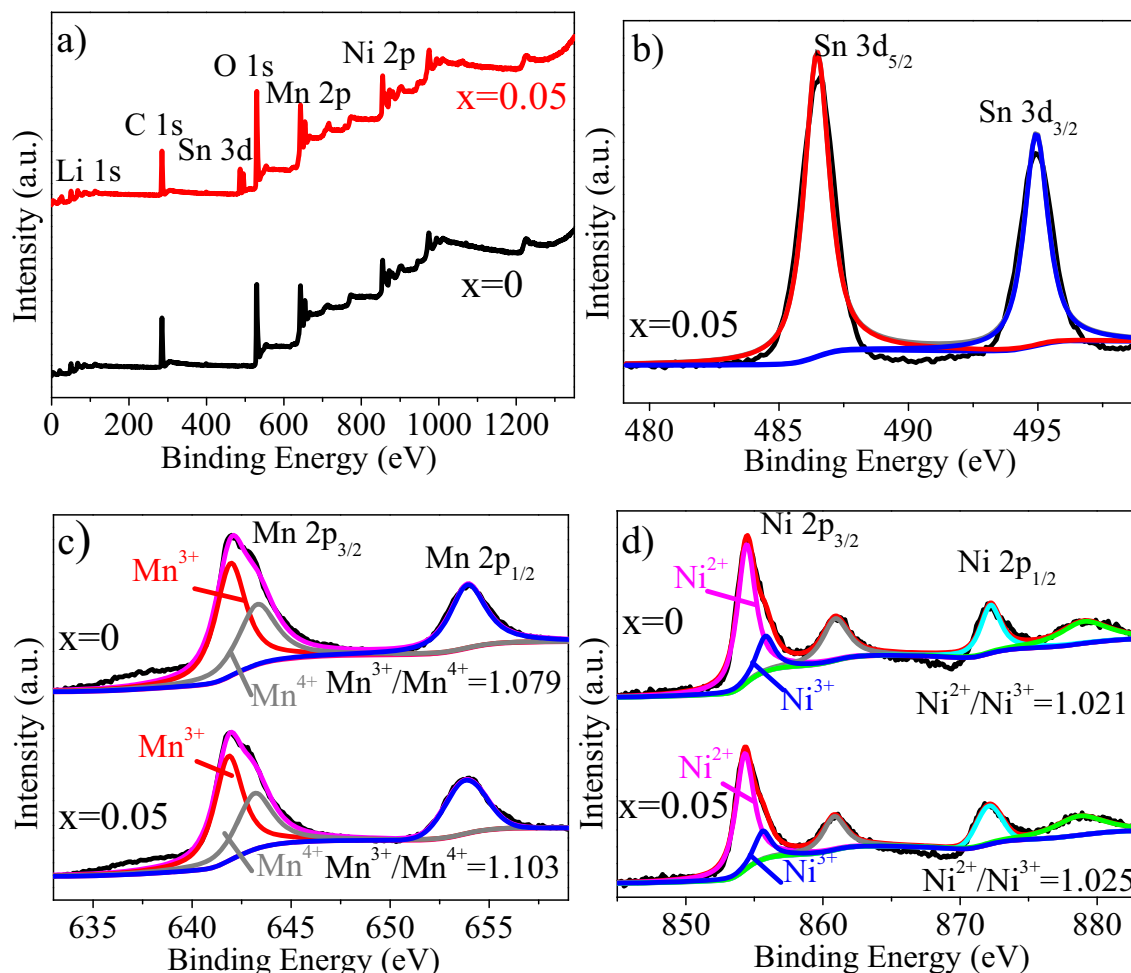
Fig. 4 XPS spectra of $Li_{1.15}Ni_{0.27}Mn_{0.58-x}Sn_xO_2$ materials with $x = 0$ and $x = 0.05$ (**a**) and corresponding spectra of Mn_{2p} (**b**), Ni_{2p} (**c**), and Sn_{3d} (**d**)

corresponds to Mn^{4+} [25], and the $2p_{3/2}$ peak at the binding energy of 854.5 eV corresponds to Ni^{2+}. Furthermore, a satellite peak commonly found in Ni-containing oxides such as $LiNiO_2$ also appears near the binding energy of Ni $2p_{3/2}$ [26–28]. Quantitative analysis of the XPS spectra of Ni2p and Mn2p shows that the ratio of Mn^{3+} and Mn^{4+} content in $Li_{1.15}Ni_{0.27}Mn_{0.58}O_2$ material is 1.079, and that in the $Li_{1.15}Ni_{0.27}Mn_{0.53}Sn_{0.05}O_2$ sample with Sn-doping amount $x = 0.05$ is 1.103. Similarly, by quantitative analysis of the XPS spectra of Ni2p, the ratios of Ni^{2+} and Ni^{3+} content in the samples with $x = 0$ and $x = 0.05$ are 1.021 and 1.025, respectively. Quantitative analysis results show that Sn doping has little effect on the valence state of transition metal elements in the material.

Electrochemical performance

Comparing the electrochemical impedance spectroscopy (EIS) results of all samples with different Sn contents in Fig. 5 (In the EIS test, when preparing electrode pads of different samples, we kept the thickness/weight of the electrode pads of each sample be consistent to exclude other factors from interfering with the test results), it is found that the electrochemical impedances of all Sn-doped $Li_{1.15}Ni_{0.27}Mn_{0.58-x}Sn_xO_2$ samples are lower than that of the pristine $Li_{1.15}Ni_{0.27}Mn_{0.58}O_2$ sample, and the $Li_{1.15}Ni_{0.27}Mn_{0.56}Sn_{0.02}O_2$ sample with $x = 0.02$ has the lowest impedance. It is worth noting that even in the optimal sample, the electrochemical impedance is higher than that of other reported materials; this can be attributed to the increase in Li/Ni cation mixing in the material. In a layered structure, the ratio of the intensity of the X-ray diffraction peaks corresponding to the (003) crystal plane and the (104) crystal plane can be used to characterize the degree of cation mixing in the structure [29]. As shown in Fig. 2, with the increase of the doping amount of Sn, the I(003)/I(104) ratio of $Li_{1.15}Ni_{0.27}Mn_{0.58-x}Sn_xO_2$ decreases continuously, indicating the degree of cation misalignment in Sn-doped samples increases, which leads to an increase in electrochemical impedance in the material.

The first charge–discharge curves of $Li_{1.15}Ni_{0.27}Mn_{0.58-x}Sn_xO_2$ materials in the range of 2–4.8 V at C/10 (1 C = 250 mAh/g) rate are shown in Fig. 6. The first charge curve of all samples consists of two parts: a slope between 3.8–4.5 V
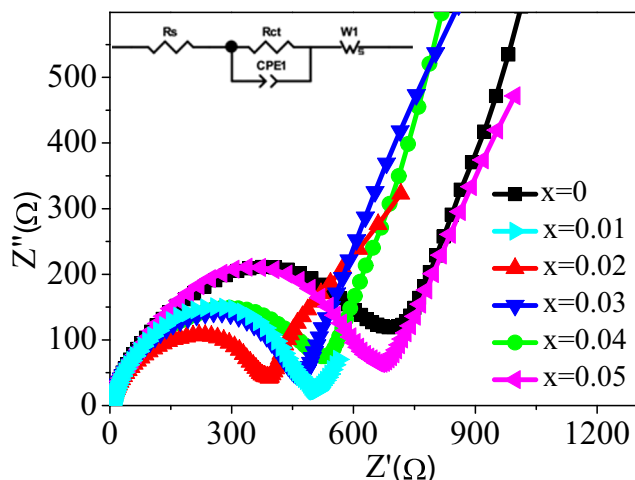
Fig. 5 Nyquist plots of samples with different Sn contents

Fig. 6 The first charge–discharge curves of $Li_{1.15}Ni_{0.27}Mn_{0.58-x}Sn_xO_2$ materials (**a**) and first specific capacity and initial efficiency of $Li_{1.15}Ni_{0.27}Mn_{0.58-x}Sn_xO_2$ materials (**b**)

and a plateau with a voltage above 4.5 V. The slope on the curve represents the oxidation process of the transition metal element in the layered structure of the material, such as the oxidation of Ni and Mn to higher valence states. The plateau above 4.5 V corresponds to the process of Li^+ deintercalation accompanied by O loss in Li_2MnO_3, which provides most of the charging capacity. After this reaction process, the Li_2MnO_3 phase is converted to electrochemically active MnO_2, which could accommodate one Li in the subsequent discharge process and then regenerate the layered $LiMnO_2$ phase. On the discharge curve of all the samples, two adjacent short voltage platforms appear between 3.5 and 2.5 V, corresponding to the reduction reaction of the transition metal ions in the layered structure and the spinel structure.

As indicated in Fig. 6b, all Sn-doped samples exhibit higher capacity and initial coulombic efficiency than the undoped $Li_{1.15}Ni_{0.27}Mn_{0.58}O_2$ sample. The $Li_{1.15}Ni_{0.27}Mn_{0.56}Sn_{0.02}O_2$ material with $x = 0.02$ shows the best performance with a discharge specific capacity of 260.8 mAh/g and initial coulombic efficiency of 84.4%, which are much higher than those of the $Li_{1.15}Ni_{0.27}Mn_{0.58}O_2$ material (210.3 mAh/g and 76.8%). However, it is worth noting that as the amount of Sn doping increases, the capacity and initial coulombic efficiency of the $Li_{1.15}Ni_{0.27}Mn_{0.58-x}Sn_xO_2$ material increase first and then decrease, and the performance of the sample with $x = 0.05$ is only slightly higher than the pristine $Li_{1.15}Ni_{0.27}Mn_{0.58}O_2$ sample. The preferred Sn-doping level is $x = 0.02$, which increases the capacity of $Li_{1.15}Ni_{0.27}Mn_{0.58-x}Sn_xO_2$ while improving the initial coulombic efficiency. Compared with ternary cathode materials containing cobalt, this discharge capacity value is slightly lower. This is because there is a serious Li/Ni cation mixing in the material. When Ni^{2+} occupies the position of Li^+ in the lithium layer, the transmission of Li^+ is hindered and part of Li^+ are unable to smoothly return to the crystal lattice, resulting in large capacity loss [30], while cobalt in the ternary material can play a role in
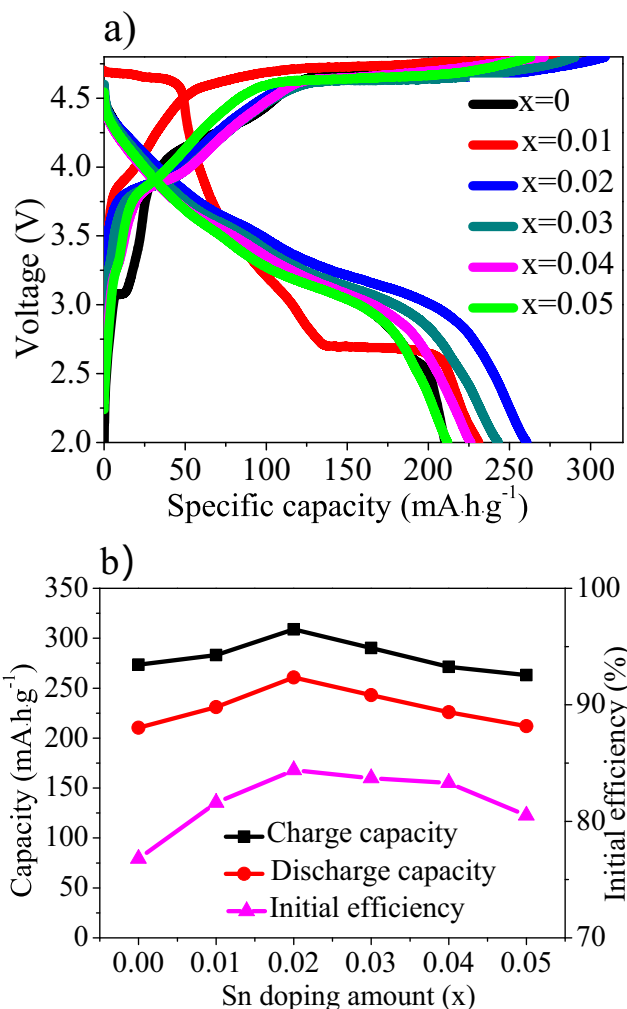
stabilizing the structure and can reduce cation mixing in the material to provide a higher discharge capacity [31].

The data in Table 1 also proves that Sn doping can effectively reduce the irreversible capacity loss of $Li_{1.15}Ni_{0.27}Mn_{0.58-x}Sn_xO_2$ material during the first charge–discharge process. According to the structural analysis of all the samples, Sn can be used as a structural support to stabilize the layered structure. Therefore, more Li^+ can be embedded back into the MnO_2 phase in the first cycle, eliminating part of the irreversible capacity loss.

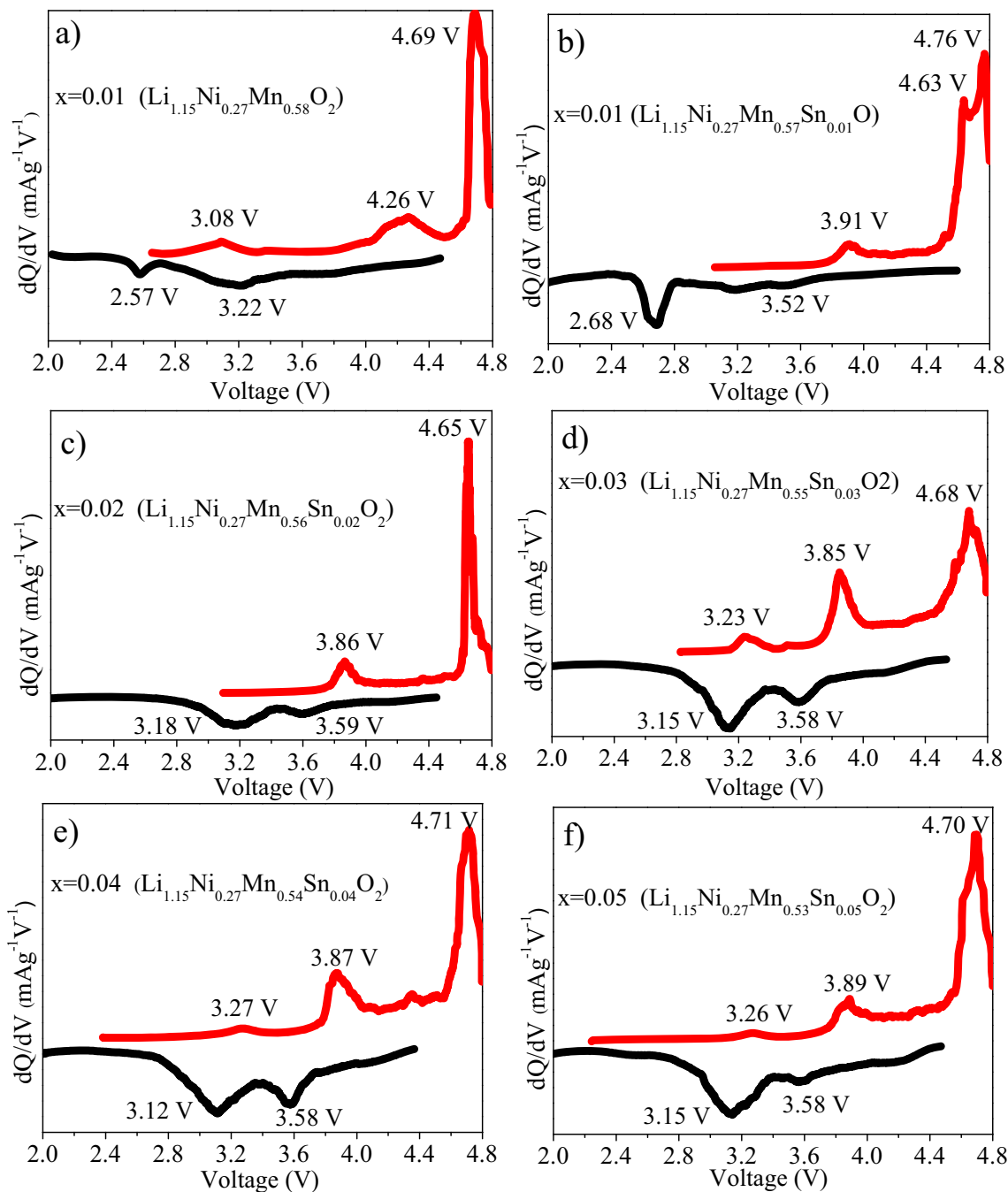The capacity differential (dQ/dV) curves of $Li_{1.15}Ni_{0.27}Mn_{0.58-x}Sn_xO_2$ cathode materials with different Sn-doping amounts are shown in Fig. 7. As can be seen from Fig. 7a, during the first charging process, the first oxidation peak appears between 2.9–3.1 V in $Li_{1.15}Ni_{0.27}Mn_{0.58}O_2$, indicating that Mn in the spinel structure phase $LiMn_2O_4$ is oxidized; when the charging voltage reaches region between 4.1 and 4.4 V, the second oxidation peak emerges. In this process, Li^+ is removed from the layered structure and oxidation of the transition metal occurs at the same time (Ni^{2+} to Ni^{4+}); when charging increases to approximately 4.6 V, a strong oxidation peak appears, which

Sn-doping amount (x)	0	0.01	0.02	0.03	0.04	0.05
1st charge capacity (mAh/g)	273.5	283.2	309	290.3	271.4	263.1
1st discharge capacity (mAh/g)	210.3	231.1	260.8	243.1	226	211.9
Irreversible capacity (mAh/g)	63.2	52.1	48.2	47.2	45.4	51.2
Initial efficiency (%)	76.8	81.6	84.4	83.7	83.3	80.5

Table 1 The first charge–discharge performance of $Li_{1.15}Ni_{0.27}Mn_{0.58-x}Sn_xO_2$ material at 0.1 C rate

corresponds to the voltage plateau on the charging curve during the first charge–discharge cycle. In this process, Li^+ is deintercalated from Li_2MnO_3 accompanied by the loss of O; then, MnO_2 generates during this reaction, and Li_2MnO_3 phase


Fig. 7 Capacity differential curves of $Li_{1.15}Ni_{0.27}Mn_{0.58-x}Sn_xO_2$ materials with different Sn-doping amounts

is activated. During the discharge process, a reduction peak arises around 3.2 V, the transition metal element ions Ni^{4+} and Mn^{4+} in the material are reduced in this process, while the reaction of Li^+ intercalation into MnO_2 occurs; the reduction peak at 2.5 V represents the reduction of Mn in the spinel phase $LiMn_2O_4$.

The dQ/dV curves of all Sn-doped samples are similar to the $Li_{1.15}Ni_{0.27}Mn_{0.58}O_2$ sample. It is worth noting that, compared with the undoped $Li_{1.15}Ni_{0.27}Mn_{0.58}O_2$ sample, the oxidation peak of transition metal ions on the dQ/dV curve of Sn-doped samples shifts to a lower voltage during the charging process, while the reduction peaks of transition metal element ions shift to higher voltages in the discharge process. This is because the doping by Sn reduces the electrochemical impedance of the $Li_{1.15}Ni_{0.27}Mn_{0.58-x}Sn_xO_2$ material [32] and enhances the electrochemical activity. However, the positions of Li and O deintercalation peaks do not change significantly, indicating that Sn doping does not affect the activity of the Li_2MnO_3 phase.
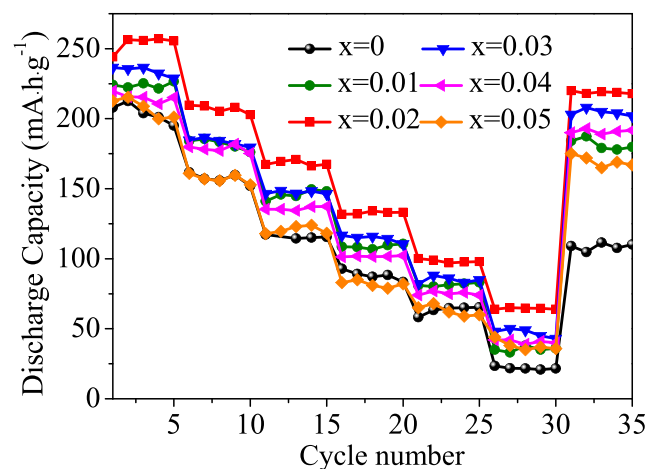
The discharge capacity of $Li_{1.15}Ni_{0.27}Mn_{0.58-x}Sn_xO_2$ material with different content of Sn in the first 100 cycles at 1 C rate is shown in Fig. 8. During the first ten cycles of Sn-doped $Li_{1.15}Ni_{0.27}Mn_{0.58-x}Sn_xO_2$ samples, the discharge capacity gradually increases, which is related to the activation process of the Li_2MnO_3 phase [8]. The $Li_{1.15}Ni_{0.27}Mn_{0.56}Sn_{0.02}O_2$ sample shows the best cycling performance without significant attenuation during 100 cycles. The discharge capacity of $Li_{1.15}Ni_{0.27}Mn_{0.56}Sn_{0.02}O_2$ after 100 cycles at 1 C is as high as 182.6 mAh/g accompanied with a capacity retention of 94.67%, while the discharge capacity of pristine $Li_{1.15}Ni_{0.27}Mn_{0.58}O_2$ is only 119.1 mAh/g after 100 cycles at 1 C accompanied with a capacity retention of 90.32%. $Li_{1.15}Ni_{0.27}Mn_{0.55}Sn_{0.03}O_2$ maintains a high specific capacity of 170.5 mAh/g after 100 cycles at the 1 C rate, and the capacity retention rate is extremely high at 98.10% among all $Li_{1.15}Ni_{0.27}Mn_{0.58-x}Sn_xO_2$ samples. $Li_{1.15}Ni_{0.27}Mn_{0.54}Sn_{0.04}O_2$ shows a discharge capacity comparable with that of $Li_{1.15}Ni_{0.27}Mn_{0.58}O_2$ sample after
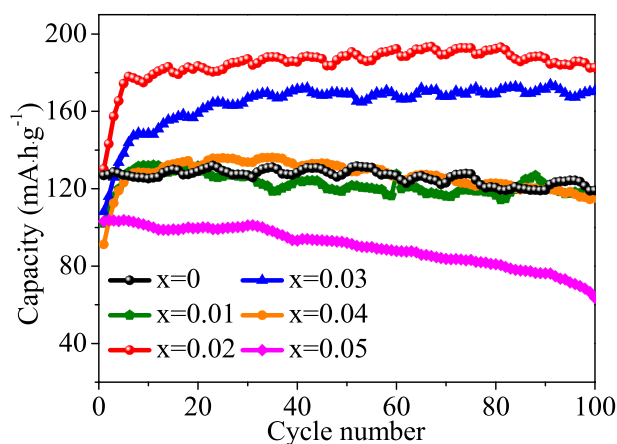
100 cycles; however, its capacity retention rate is inferior to that of the undoped sample. $Li_{1.15}Ni_{0.27}Mn_{0.53}Sn_{0.05}O_2$ delivers a discharge specific capacity of only 63.5 mAh/g after 100 cycles at 1 C, and its capacity retention rate is the lowest among all samples, only 61.18%. According to above analysis, an appropriate Sn content can improve structural stability of $Li_{1.15}Ni_{0.27}Mn_{0.58-x}Sn_xO_2$ materials, which increases their cycle performances, although excessive Sn doping can degrade the cycle performance of $Li_{1.15}Ni_{0.27}Mn_{0.58-x}Sn_xO_2$ material. These results are in good agreement with the conclusion of the previous material structure characterization.

Figure 9 shows the rate performance of all $Li_{1.15}Ni_{0.27}Mn_{0.58-x}Sn_xO_2$ samples. It is illustrated that the rate capability of $Li_{1.15}Ni_{0.27}Mn_{0.58-x}Sn_xO_2$ material has been significantly improved due to Sn doping, and the $Li_{1.15}Ni_{0.27}Mn_{0.56}Sn_{0.02}O_2$ sample exhibits the best rate performance among all samples. $Li_{1.15}Ni_{0.27}Mn_{0.56}Sn_{0.02}O_2$ sample shows a discharge capacity of approximately 65 mAh/g at 5 C, which is three times that of the undoped $Li_{1.15}Ni_{0.27}Mn_{0.58}O_2$. Additionally, when the current density returns to 0.1 C, the $Li_{1.15}Ni_{0.27}Mn_{0.56}Sn_{0.02}O_2$ sample acquires a specific discharge capacity of 220 mAh/g, which is nearly twice that of $Li_{1.15}Ni_{0.27}Mn_{0.58}O_2$. By investigating the rate capability of various Sn-doped samples at different current densities, the proper content of Sn doping ($x = 0.02$) can effectively promote the rate capability of $Li_{1.15}Ni_{0.27}Mn_{0.58-x}Sn_xO_2$ materials, but excessive Sn doping is detrimental to the rate capability of the material. The specific discharge capacity of $Li_{1.15}Ni_{0.27}Mn_{0.53}Sn_{0.05}O_2$ at 5 C is only half that of $Li_{1.15}Ni_{0.27}Mn_{0.57}Sn_{0.01}O_2$, and the discharge capacity is only approximately 170 mAh/g when the current density returns to 0.1 C. It is concluded that Sn doping can significantly improve the rate capability of $Li_{1.15}Ni_{0.27}Mn_{0.58-x}Sn_xO_2$, which is related to the change in the material structure. The structural characterization of $Li_{1.15}Ni_{0.27}Mn_{0.58-x}Sn_xO_2$ materials has proven that Sn doping increases the interplanar spacing of

Fig. 8 Discharge capacity of $Li_{1.15}Ni_{0.27}Mn_{0.58-x}Sn_xO_2$ cathode material with different Sn-doping amounts in the first 100 cycles at a 1 C rate

Fig. 9 Comparison of rate capability of $Li_{1.15}Ni_{0.27}Mn_{0.58-x}Sn_xO_2$ materials with different Sn-doping amounts

the monoclinic and hexagonal layered structures in $Li_{1.15}Ni_{0.27}Mn_{0.58-x}Sn_xO_2$ materials, which are more conducive to the transport of lithium ions. In addition, Sn ions can be used as a support to stabilize the material structure to maintain the structural stability during charge–discharge processes.

Conclusions

$Li_{1.15}Ni_{0.27}Mn_{0.58-x}Sn_xO_2$ samples with different Sn content were prepared by the solvothermal method. Structural analysis shows that a small amount of Sn doping ($x \leq 0.02$) does not introduce impurities into the material, but when the content of Sn exceeds 0.03, Li_2SnO_3 impurity phases begin to appear in the material. With increasing Sn content, the main diffraction peaks of (003) and (104) in the XRD pattern shift to a small angle, indicating that the crystal plane spacing of the monoclinic-layered structure and the hexagonal layered structure in $Li_{1.15}Ni_{0.27}Mn_{0.58-x}Sn_xO_2$ increases, which is also confirmed by TEM characterization results. The particles of $Li_{1.15}Ni_{0.27}Mn_{0.58-x}Sn_xO_2$ are microspheres composed of primary particles around 40 nm. There are many pores on the spherical particles, which are beneficial to the penetration of the electrolyte and diffusion of lithium ions.

All Sn-doped samples show higher discharge capacities and initial coulombic efficiencies than those of pristine $Li_{1.15}Ni_{0.27}Mn_{0.58}O_2$ cathode material. $Li_{1.15}Ni_{0.27}Mn_{0.56}Sn_{0.02}O_2$ reached the highest discharge capacity of 260.8 mAh/g in the first cycle at 0.1 C, and its first coulombic efficiency was as high as 84.4%. During the 100 cycles at the 1 C rate, it is demonstrated that the proper Sn-doping content ($x \leq 0.02$) can simultaneously improve the discharge capacity and cycle retention of $Li_{1.15}Ni_{0.27}Mn_{0.58-x}Sn_xO_2$ cathode materials; however, excess Sn doping ($x > 0.03$) deteriorates cycle performance. $Li_{1.15}Ni_{0.27}Mn_{0.56}Sn_{0.02}O_2$ maintains the highest discharge specific capacity of 182.6 mAh/g after 100 cycles at the 1 C rate, and the capacity retention rate is also high (94.67%); $Li_{1.15}Ni_{0.27}Mn_{0.55}Sn_{0.03}O_2$ shows the highest capacity retention among all samples after 100 cycles (98.1%), while holding a high discharge specific capacity of 170.5 mAh/g. The improvement in the rate capability of $Li_{1.15}Ni_{0.27}Mn_{0.58-x}Sn_xO_2$ material due to Sn doping is particularly significant. The discharge specific capacity of $Li_{1.15}Ni_{0.27}Mn_{0.56}Sn_{0.02}O_2$ at 5 C is three times that of the undoped $Li_{1.15}Ni_{0.27}Mn_{0.58}O_2$ material. In addition, when the current density returns to 0.1 C, the $Li_{1.15}Ni_{0.27}Mn_{0.56}Sn_{0.02}O_2$ sample still shows a high discharge capacity of 220 mAh/g.

The conclusions in this study demonstrate that Sn doping can increase the interplanar spacing of the layered structure in $Li_{1.15}Ni_{0.27}Mn_{0.58-x}Sn_xO_2$ cathode material and reduce the

electrochemical impedance; thus, the electrochemical performance of the cathode material is comprehensively improved.

References

1. Xu CS, Jiang WF, Yu HT, Guo CF, Xie Y, Ren N, Yi TF (2019) Hollow and hierarchical $Li_{1.2}Mn_{0.54}Ni_{0.13}Co_{0.13}O_2$ micro-cubes as promising cathode materials for lithium ion battery. J Alloys Compd 807:151686
2. Li X, Qian K, He YB, Liu C, An D, Li Y, Kang F (2017) A dual-functional gel-polymer electrolyte for lithium ion batteries with superior rate and safety performances. J Mater Chem A 5:18888–18895
3. Yi TF, Zhu YR, Tao W, Luo S, Xie Y, Li XF (2018) Recent advances in the research of $MLi_2Ti_6O_{14}$ (M= 2Na, Sr, Ba, Pb) anode materials for Li-ion batteries. J Power Sources 399:26–41
4. Yi TF, Wei TT, Li Y, He YB, Wang ZB (2020) Efforts on enhancing the Li-ion diffusion coefficient and electronic conductivity of titanate-based anode materials for advanced Li-ion batteries. Energy Storage Materials
5. Liu C, Qian K, Lei D, Li B, Kang F, He YB (2017) Deterioration mechanism of $LiNi_{0.8}Co_{0.15}Al_{0.05}O_2$/graphite-$SiO_x$ power batteries under high temperature and discharge cycling conditions. Journal of Materials Chemistry A:6
6. An J, Shi L, Chen G, Li M, Liu H, Yuan S, Zhang D (2017) Insights into the stable layered structure of a Li-rich cathode material for lithium-ion batteries. J Mater Chem A 5(37):19738–19744
7. Xie D, Li G, Li Q, Fu C, Fan J, Li L (2016) Improved cycling stability of cobalt-free Li-rich oxides with a stable interface by dual doping. Electrochim Acta 196:505–516
8. Ye D, Sun C, Chen Y, Ozawa K, Hulicova-Jurcakova D, Zou J, Wang L (2015) Ni-induced stepwise capacity increase in Ni-poor Li-rich cathode materials for high performance lithium ion batteries. Nano Res 8(3):808–820
9. Liu Y, Gao Y, Wang Q, Dou (2014) A influence of coated MnO_2 content on the electrochemical performance of $Li_{1.2}Ni_{0.2}Mn_{0.6}O_2$ cathodes. Ionics 20.6: 825–831
10. Liu Y, Zhang Z, Gao Y, Yang G, Li C, Zheng J, Su M (2016) Mitigating the voltage decay and improving electrochemical properties of layered-spinel $Li_{1.1}Ni_{0.25}Mn_{0.75}O_{2.3}$ cathode material by Cr doping. J Alloys Compd 657:37–43
11. Pan L, Xia Y, Qiu B, Zhao H, Guo H, Jia K, Liu Z (2016) Structure and electrochemistry of B doped $Li(Li_{0.2}Ni_{0.13}Co_{0.13}Mn_{0.54})_{1-x}B_xO_2$ as cathode materials for lithium-ion batteries. J Power Sources 327:273–280
12. Jin X, Xu Q, Liu H, Yuan X, Xia Y (2014) Excellent rate capability of Mg doped $Li[Li_{0.2}Ni_{0.13}Co_{0.13}Mn_{0.54}]O_2$ cathode material for lithium-ion battery. Electrochim Acta 136:19–26
13. Li X, Xin H, Liu Y, Li D, Yuan X, Qin X (2015) Effect of niobium doping on the microstructure and electrochemical properties of lithium-rich layered $Li[Li_{0.2}Ni_{0.2}Mn_{0.6}]O_2$ as cathode materials for lithium ion batteries. RSC Adv 5(56):45351–45358

14. Li N, An R, Su Y, Wu F, Bao L, Chen L, Chen S (2013) The role of yttrium content in improving electrochemical performance of layered lithium-rich cathode materials for Li-ion batteries. J Mater Chem A 1(34):9760–9767

15. Zhao J, Wang Z, Guo H, Li X, He Z, Li T (2015) Synthesis and electrochemical characterization of Zn-doped Li-rich layered Li[Li$_{0.2}$Mn$_{0.54}$Ni$_{0.13}$Co$_{0.13}$]O$_2$ cathode material. Ceram Int 41(9):11396–11401

16. Chen H, Hu Q, Huang Z, He Z, Wang Z, Guo H, Li X (2016) Synthesis and electrochemical study of Zr-doped Li[Li$_{0.2}$Mn$_{0.54}$Ni$_{0.13}$Co$_{0.13}$]O$_2$ as cathode material for Li-ion battery. Ceram Int 42(1):263–269

17. Fu F, Xu GL, Wang Q, Deng YP, Li X, Li JT, Sun SG (2013) Synthesis of single crystalline hexagonal nanobricks of LiNi$_{1/3}$Co$_{1/3}$Mn$_{1/3}$O$_2$ with high percentage of exposed {010} active facets as high rate performance cathode material for lithium-ion battery. J Mater Chem A 1(12):3860–3864

18. Wang C C, Jarvis K A, Ferreira P J, Manthiram (2013) A effect of synthesis conditions on the first charge and reversible capacities of lithium-rich layered oxide cathodes. Chem Mater 25.15: 3267–3275

19. Ho CS, Kang YC (2014) Uniform decoration of vanadium oxide nanocrystals on reduced graphene-oxide balls by an aerosol process for lithium-ion battery cathode material. Chem Eur J 20(21):6294–6299

20. Mohanty D, Sefat AS, Kalnaus S, Li J, Meisner RA, Payzant EA, Daniel C (2013) Investigating phase transformation in the Li$_{1.2}$Co$_{0.1}$Mn$_{0.55}$Ni$_{0.15}$O$_2$ lithium-ion battery cathode during high-voltage hold (4.5 V) via magnetic, X-ray diffraction and electron microscopy studies. J Mater Chem A 1(20):6249–6261

21. Mohanty D, Sefat AS, Li J, Meisner RA, Rondinone AJ, Payzant EA, Daniel C (2013) Correlating cation ordering and voltage fade in a lithium-manganese-rich lithium-ion battery cathode oxide: a joint magnetic susceptibility and TEM study. Phys Chem Chem Phys 15(44):19496–19509

22. Jung SK, Gwon H, Hong J, Park KY, Seo DH, Kim H, Kang K (2014) Understanding the degradation mechanisms of LiNi$_{0.5}$Co$_{0.2}$Mn$_{0.3}$O$_2$ cathode material in lithium ion batteries. Advanced Energy Materials 4.1:1300787

23. Li J, He X, Zhao R, Wan C, Jiang C, Xia D, Zhang S (2006) Stannum doping of layered LiNi$_{3/8}$Co$_{2/8}$Mn$_{3/8}$O$_2$ cathode materials with high rate capability for Li-ion batteries. J Power Sources 158(1):524–528

24. Zheng Z, Hua WB, Yu C, Zhong YJ, Xu BB, Wang JZ, Zhang ZY (2015) Heterogeneous intergrowth xLi$_{1.5}$Ni$_{0.25}$Mn$_{0.75}$O$_{2.5}$·(1-x)Li$_{0.5}$Ni$_{0.25}$Mn$_{0.75}$O$_2$ (0≤ x≤ 1) composites: synergistic effect on electrochemical performance. Dalton Trans 44(32):14255–14264

25. Nakayama M, Watanabe K, Ikuta H, Uchimoto Y, Wakihara M (2003) Grain size control of LiMn$_2$O$_4$ cathode material using microwave synthesis method. J Solid State Ionics 164(1–2):35–42

26. Shaju KM, Rao GVS, Chowdari BVR (2003) X-ray photoelectron spectroscopy and electrochemical behaviour of 4 V cathode, Li(Ni$_{1/2}$Mn$_{1/2}$)O$_2$. Electrochim Acta 48(11):1505–1514

27. Carley AF, Jackson SD, O'shea JN, Roberts MW (1999) The formation and characterisation of Ni^{3+}-an X-ray photoelectron spectroscopic investigation of potassium-doped Ni (110)-O. Surf Sci 440(3):L868–L874

28. Amine K, Tukamoto H, Yasuda H, Fujita Y (1996) A new three-volt spinel Li$_{1+x}$Mn$_{1.5}$Ni$_{0.5}$O$_4$ for secondary lithium batteries. J Electrochem Soc 143(5):1607–1613

29. Wang CC, Jarvis KA, Ferreira PJ, Manthiram A (2013) Effect of synthesis conditions on the first charge and reversible capacities of lithium-rich layered oxide cathodes. Chem Mater 25(15):3267–3275

30. Xia H, Liu C, Shen L, Yu J, Li B, Kang F, He YB (2020) Structure and thermal stability of LiNi$_{0.8}$Co$_{0.15}$Al$_{0.05}$O$_2$ after long cycling at high temperature. J Power Sources 450:227695

31. He YS, Pei L, Liao XZ, Ma ZF (2008) Preparation and performance of LiNi$_{0.8}$Co$_{0.2}$O$_2$ cathode material based on co-substituted α-Ni(OH)$_2$ precursor. Chin Sci Bull 09:46–50

32. Chen H, Hu Q, Peng W, Guo H, Yan G, Wu X (2017) New insight into the modification of Li-rich cathode material by stannum treatment. Ceram Int 43(14):10919–10926